catalysts

MDPI

Article

Direct Construction of K-Fe_3C@C Nanohybrids Utilizing Waste Biomass of Pomelo Peel as High-Performance Fischer–Tropsch Catalysts

Songbai Qiu [1,2,3,†], Jianfeng Chen [1,†], Yujian Fan [1], Zan Huang [1], Qingwei Meng [1,2,3], Liang Ma [1,2,3], Qian Zhang [1,2,3,*] and Tiejun Wang [1,2,3,*]

[1] School of Chemical Engineering and Light Industry, Guangdong University of Technology, Guangzhou 510006, China; qiusb@gdut.edu.cn (S.Q.); jianfengchen2022@163.com (J.C.); fanyujianx@163.com (Y.F.); huangzanhh@163.com (Z.H.); qwmeng@gdut.edu.cn (Q.M.); maliangs@gdut.edu.cn (L.M.)
[2] Guangdong Provincial Key Laboratory of Plant Resources Biorefinery, Guangzhou 510006, China
[3] Guangzhou Key Laboratory of Clean Transportation Energy and Chemistry, Guangzhou 510006, China
* Correspondence: zhangqian@gdut.edu.cn (Q.Z.); tjwang@gdut.edu.cn (T.W.)
† These authors contributed equally to this work.

Abstract: As the only renewable organic carbon source, abundant biomass has long been established and developed to mass-produce functionalized carbon materials. Herein, an extremely facile and green strategy was executed for the first time to in situ construct K-Fe_3C@C nanohybrids directly by one-pot carbonizing the pomelo peel impregnated with $Fe(NO_3)_3$ solutions. The pyrolytically self-assembled nanohybrids were successfully applied in Fischer–Tropsch synthesis (FTS) and demonstrated high catalytic performance. Accordingly, the optimized K-Fe_3C@C catalysts revealed excellent FTS activity (92.6% CO conversion) with highlighted C_{5+} hydrocarbon selectivity of 61.3% and light olefin ($C_{2-4}^{=}$) selectivity of 26.0% (olefin/paraffin (O/P) ratio of 6.2). Characterization results further manifest that the high performance was correlated with the in situ formation of the core-shell nanostructure consisting of Fe_3C nanoparticles enwrapped by graphitized carbon shells and the intrinsic potassium promoter originated in pomelo peel during high-temperature carbonization. This work provided a facile approach for the low-cost mass-fabrication of high-performance FTS catalysts directly utilizing waste biomass without any chemical pre-treatment or purification.

Keywords: pomelo peel; iron carbides; core-shell structure; Fischer–Tropsch catalyst; potassium promoter

Citation: Qiu, S.; Chen, J.; Fan, Y.; Huang, Z.; Meng, Q.; Ma, L.; Zhang, Q.; Wang, T. Direct Construction of K-Fe_3C@C Nanohybrids Utilizing Waste Biomass of Pomelo Peel as High-Performance Fischer–Tropsch Catalysts. *Catalysts* **2022**, *12*, 542. https://doi.org/10.3390/catal12050542

Academic Editor: Jaehoon Kim

Received: 15 April 2022
Accepted: 10 May 2022
Published: 16 May 2022

1. Introduction

As of now, FTS has attracted renewed attention as a well-known and long-established commercial technical route to produce a wide range of synthetic paraffins and olefins from syngas comprising primarily H_2 and CO, derived from non-petroleum carbon sources, such as coal, biomass and natural gas [1–4]. In particular, for coal-based FTS processes with low H_2/CO ratio syngas, iron-based catalysts are preferentially applied in industrial implementation, depending largely on abundant reserves, low price, adequate catalytic performance for H_2-poor syngas and impressive selectivity for α-olefin production [5–7].

According to plentiful theoretical and experimental reports, various iron carbide phases, mainly involving θ-Fe_3C, χ-Fe_5C_2, ε-Fe_2C/ε'-$Fe_{2.2}C$ and Fe_7C_3, have been traditionally regarded as the intrinsic active sites of Fe-based FTS catalysts [8–10]. Among them, thermodynamically stable θ-Fe_3C cementite has been confirmed to represent superior C-C chain growth ability under realistic FTS conditions [11]. Currently, a series of strategies have been pursued to directly synthesize iron carbides employed as efficient FTS catalysts, utilizing the wet-chemical technique, solid-state reaction, sol–gel processing, chemical vapor deposition, plasma or laser pyrolysis, metal–organic-framework-templated

strategy, etc. [6,12–19]. Nonetheless, for practical application, these approaches still encounter many obstacles and restrictions accompanying multiple-step, complicated and poor scaling-up procedures, together with hazardous or costly organic carbon sources. Therefore, the rational design of a synthesis strategy appears more attractive for the facile and scalable fabrication of iron carbides via controlling the starting precursors of low-cost carbon sources.

Being the only renewable organic carbon source, abundant biomass has long been established as a sustainable alternative for substituting fossil carbon sources in the large-scale production of functionalized carbon materials [20–22]. Employing characteristic properties of biomass materials in terms of special composition and hierarchical structure, plenty of the newly developing applications of biomass waste using facile and green processing steps have been reported to yield effective biomass-derived heterogeneous catalysts including cellulose-based catalysts, lignin-derived catalysts, ash-based catalysts, biochar-based catalysts, biochar-supported catalysts, biomass-derived electrocatalysts, biochar-solid acids, etc. [22–24]. Nevertheless, the existing valorization of biomass wastes frequently involves various types of pre-treatments, purification and activation technologies in the form of physical, chemical and biological processes, which could reduce the economic attractiveness and technical viability due to high-cost and multiple, complicated procedures.

With the heavy consumption of pomelo fruit cultivated widely around the world, large amounts of pomelo peel waste are inevitably produced as a low-value by-product, with a global output of approximately 2.8–4.7 million tons in 2018 [25]. Pomelo peel mainly consists of pectin, cellulose, soluble sugars, hemicellulose, mineral elements and lignin (Table S1), accumulating in plant growth stages via photosynthesis [26–28]. Among metal elements present in pomelo peel, potassium is the most abundant nutrient, ensuring plant growth–metabolism balance [29]. Owing to abundant required elements and special coordination environments, pomelo peel has commercial potential for manufacturing porous carbon materials such as supercapacitors, adsorbents, sensing material, etc. [30–34], as well as fabricating heterogeneous catalysts, such as Cu/C catalyst [35], hierarchically porous $LaFeO_3$ perovskite [36], etc. However, to date, the synergistic effect of mineral elements in pomelo peel has never been investigated as intrinsic promoters of heterogeneous catalysts.

In this study, for the first time, low-value pomelo peel without any chemical treatment or purification, serving as the abundant renewable carbon source and potassium source, was directly utilized to in situ construct the high-performance K-Fe_3C@C catalysts for FTS through Fe impregnation and carbonization. The organic constituents rich in oxygen-containing groups in pomelo peel could interact with Fe precursor via complexation, resulting in self-fabrication into three-dimensional organic–inorganic hybrid precursors during Fe impregnation. Subsequent carbonization procedures not only promoted the formation of core-shell structural Fe_3C embedded in graphitic shells, owing to the graphitization of its organic components, but also led to the migration of K accumulated in pomelo peel onto the surface of final nanohybrids. Furthermore, the effects of critical factors including additive amounts of ferric nitrate, carbonization temperature and biomass types on the catalytic properties were carefully revealed and characterized by various analysis techniques. Accordingly, the synergetic catalysis between core-shell structural Fe_3C and self-doped K-promoter has been proven to be responsible for the high FTS performance in controlling the transformation of syngas into desired light olefins and C_{5+} hydrocarbons. This work could demonstrate a bright prospect for natural biomass in the direct fabrication of high-performance carbon-based catalysts on the basis of composition characteristics in plant tissues.

2. Results and Discussion

2.1. Characterization of the Catalysts

Herein, pomelo peel, a type of waste natural biomass, was employed as a renewable carbon source to directly fabricate K-Fe_3C@C nanohybrids through an extremely facile impregnation–carbonization process. As shown in Figure 1A, the carbonization temper-

ature was a key factor in controlling the chemical structure and properties of Fe@C-1.0 nanohybrids (the so-called Fe@C-1.0 indicated that the mass ratio of dried pomelo peel to $Fe(NO_3)_3 \cdot 9H_2O$ was equal to 1.0 during impregnation). When the carbonization temperature was below 600 °C, a cluster of weak peaks at 36.0°, 41.9°, 60.8° were attributed to the FeO phase (JCPDS no. 06-0615). With further heating up to 650 °C, the broadened diffraction peak located at around 26.3°could be indexed to graphitic carbon (JCPDS no. 41-1487), indicating that the graphitization degree was enhanced with the increasing carbonization temperature. The α-Fe (JCPDS no. 06-0696) was assigned by diffraction peaks at 44.7° and 65.0°, accompanied by the emergence of θ-Fe_3C species. After carbonization at 700 °C, the θ-Fe_3C phases (JCPDS no. 35-0772) were assigned by a series of characteristic peaks at 37.7°, 42.9°, 43.7°, 45.0°, 45.9°, 49.1°, 58.0°, 70.9°, 77.9° and 78.6°. The intensity of correlated reflections clarified that the well-crystallized θ-Fe_3C phase became the major iron species. Meanwhile, the over-high carbonization temperature exceeding 850 °C resulted in the crystal phase transformation from Fe_3C to Fe. Consequently, 700 °C was adopted as the optimized carbonization temperature.

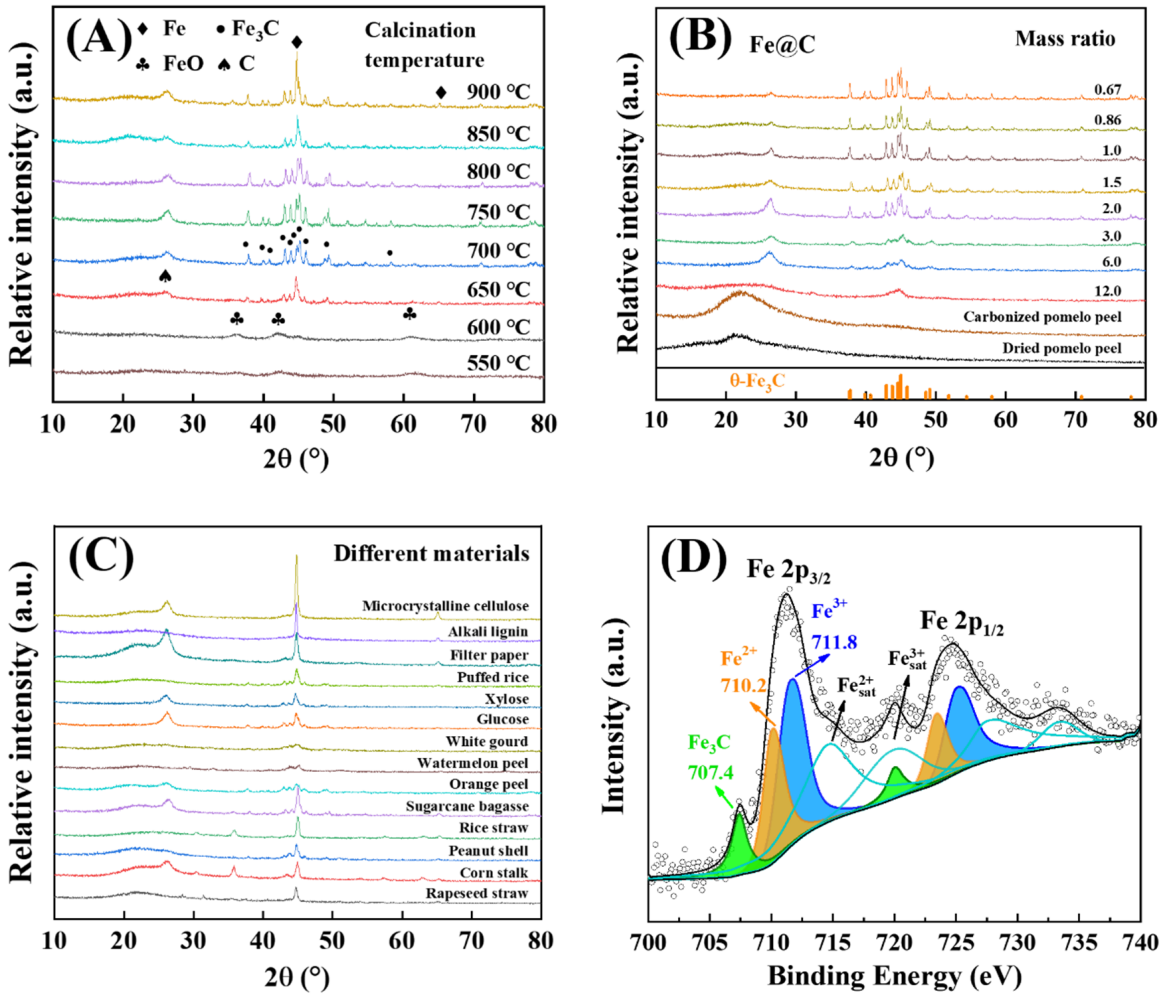

Figure 1. XRD patterns of (**A**) Fe@C-1.0 with various calcination temperatures, (**B**) dried pomelo peel and as-prepared Fe@C-*x* with different mass ratio after carbonization at 700 °C and (**C**) iron-impregnated different biomass materials after carbonization at 700 °C; (**D**) XPS survey spectrum of Fe@C-1.0 sample.

Figure 1B presents the XRD patterns of Fe@C nanohybrids with a different mass ratio of dried pomelo peel to $Fe(NO_3)_3 \cdot 9H_2O$ (0.67~12.0) after carbonization at 700 °C. The amorphous carbon existed at about 22.5°. With the introduction of ferric nitrate, θ-Fe_3C began to emerge in the samples, accompanied by the coexistence of the diffraction peaks of graphite

carbon. Apparently, the diffraction intensity of dominant Fe_3C phases gradually heightened with increasing impregnation amounts of ferric nitrate [37]. Additionally, the subsequent TEM observations further confirmed the formation of the core-shell structure consisting of inner Fe_3C nanoparticles as cores and graphite carbon as shells. Therefore, it clearly demonstrated that pomelo peel without any chemical treatment or further purification was successfully applied in in situ fabrication of Fe_3C@C core-shell nanohybrids through carbothermal reductions and interfacial reactions during high-temperature carbonization. In the carbonized samples, no other XRD signals were detected for the presence of a very small quantity of mineral elements, even though they were really found in the natural biomass (Table S2).

Figures 1C and S3 display the corresponding XRD patterns of the Fe@C samples obtained from different biomass feedstocks as organic carbon precursors without any chemical treatment. The relevant preparation process was kept consistent with the procedures involved above, following the mass ratio of 3.0 of dried bio-materials to ferric nitrate. For simplicity, a variety of biomass-derived Fe@C samples were denoted as biomass name, respectively. Over the period of high-temperature pyrolysis (700 °C), the iron precursors originating from various carbon resources were primarily transformed into Fe_3C and α-Fe species, except sometimes a small quantity of FeO and Fe_3O_4. The formation of the Fe_3C phase was facilitated by pomelo peel, orange peel, watermelon peel, white gourd, aloe pulp, water hyacinth, water moss, peanut shell, sugarcane bagasse, xylose, glucose and puffed rice, while the α-Fe phase occurred mainly in the case of rapeseed straw, corn stalk, rice straw, filter paper, alkali lignin and microcrystalline cellulose. Therefore, during high-temperature carbonization, the precursor categories chosen exerted an important influence on the physicochemical properties of the final products, which was probably caused by the complex structural components comprising cellulose, hemicellulose, lignin, simple sugars, starch, crude fat, pectic substances and proteins, inorganic minerals, etc. [22,38]. The Fe 2p XPS spectrum of the Fe@C-1.0 sample carbonized at 700 °C was examined to identify the chemical states of Fe species (Figure 1D). Two obvious peaks located at ~724.7 and ~711.2 eV corresponded to Fe_3O_4 in the final product of K-Fe_3C@C nanohybrids, indicating the occurrence of surface oxidation due to air exposure [39,40]. Meanwhile, it was noteworthy that other coexistent peaks at ~720.1 eV and ~707.4 eV belonged to Fe_3C species, according to the previous studies, which agreed well with the above XRD analysis [41]. Additionally, Mössbauer spectroscopy was employed for identifying and quantifying the exact phase compositions of iron species (Figure 2 and Table 1). In the Fe@C-1.0 catalyst, iron species appeared mainly in the form of 75.2% θ-Fe_3C and 18.0% α-Fe, both of which had been proven as active phases of FTS catalysts. The results further provide clear evidence for the dominant formation of Fe_3C species after carbonization.

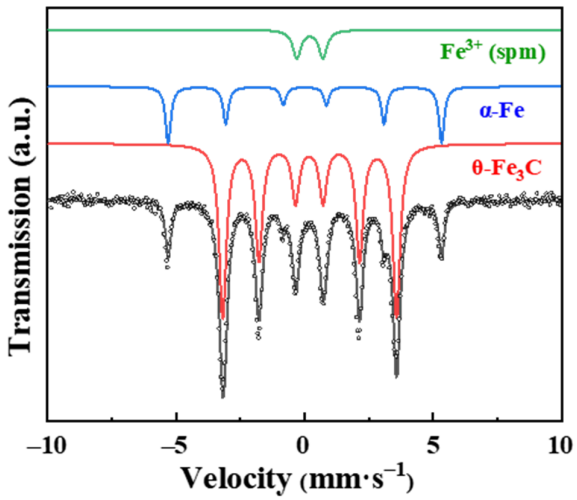

Figure 2. The ^{57}Fe Mössbauer spectra of the Fe@C-1.0 sample.

Table 1. The ^{57}Fe Mössbauer Parameters of the Fe@C-1.0 sample.

Sample	Phase	IS ($mm \cdot s^{-1}$)	QS ($mm \cdot s^{-1}$)	H (kOe)	Spectral Contribution (%)
Fe@C-1.0	θ-Fe_3C	0.19	0.02	210	75.2
	α-Fe	0.01	-	330	18.0
	Fe^{3+} (spm)	0.20	1.01	-	6.9

SEM and TEM techniques were utilized to acquire detailed information about the surface morphology and structure of pomelo peel and its supported iron catalysts in Figures 3 and S4. As shown in Figure 3A–B, the dried pomelo peel had a smooth and clean layered surface, while carbonized pomelo peel not only kept the layered surface but had numerous small spherical nanoparticles, exposed on its external surface. In terms of EDS analysis (Figure S4A), besides the primary elements of carbon and oxygen, some inorganic elements, such as Mg, Al, Si, K, Ca, etc., were detected, implying that the inorganic constituents accumulated in pomelo peel could migrate and redistribute onto the surface of corresponding biochar during high-temperature carbonization [42]. After carbonizing the iron-impregnated pomelo peel, the Fe@C-1.0 sample was characteristic of the rough surface and porous microstructure in Figures 3C–J and S4B, owing to the in situ formation of iron carbide nanoparticles. Furthermore, the HRTEM image in Figure 3F represented the distinct lattice fringes with interplanar spacings of 0.34 and 0.20 nm, corresponding to the graphite (002) and Fe_3C (220) crystal plane, respectively. Figure 3E,F distinctly demonstrated the appearance of the core-shell Fe_3C nanoparticles encapsulated in graphitized carbon shells. The elemental mapping images of C, Fe and K, over the sample of Fe@C-1.0, verified that the K element was distributed uniformly on the carbon matrix. Considering all of this, combined with the characterization results in ICP-OES, it was validated further that the K element rich in pomelo peel could migrate, aggregate and precipitate onto the biochar surface and self-doped into the final products as alkali promoters through the one-pot pyrolysis strategy.

The textural properties of typical Fe@C samples with different Fe loading were evaluated by the N_2 adsorption/desorption isotherms (Figures 4 and S5), and the relevant results are summarized in Table 2. The actual Fe and K loadings of the as-synthesized samples were established using ICP-OES analysis. The four Fe@C samples with Fe loadings in the range of 13.5–47.2 wt% displayed type-IV hysteresis loops, indicating the existence of mesopore structure. After incorporation with Fe, significant enlargement in specific surface area and porosity was observed. For instance, compared with the carbonized pomelo peel, the BET specific surface area of Fe@C samples was augmented from 1.5 to 48.1–91.0 $m^2 \cdot g^{-1}$, indicating that the addition of an iron source was beneficial to the graphitization reaction of pomelo peel and the creation of a carbon matrix and abundant porosities. Meanwhile, the Raman spectra of the carbonized samples are shown in Table 2 and Figure S6 for estimating the graphitization degree. Correspondingly, the correlative intensity ratios of I_D/I_G (D-band and G-band) decreased gradually with the increasing Fe loadings, which indicated that the Fe loadings played important roles in the graphitization process [43].

Moreover, TG-DSC measurements were executed to monitor the carbonization process of pomelo peel and the precursor of Fe@C-1.0, as shown in Figure 5. The incipient mass loss began to proceed below 150 °C, mostly owing to the evaporation of free and bound water. The steep stage of the mass loss curve within 150–400 °C resulted from the pyrolysis degradation of oxygenated organic constituents in pomelo peel, accompanied by the gas evolution of CO_2, CO, H_2O, CH_4, etc. [35,44]. After the introduction of iron species, the maximum rate of weight loss happened at 321 °C, which was linked to the decomposition of ferric nitrate, and meanwhile, another weight loss peak located at 500–700 °C was assigned to the carbothermal reductions and interfacial reactions among the deoxidized iron species and adjacent carbonized biochar [45], thereby leading to the progressive formation of Fe_3C. Compared with the precursor of Fe@C-1.0, the original decomposition peaks of

pomelo peel that occurred at 208 °C and 327 °C shifted toward the higher temperature side corresponding to 280 °C and 370 °C. This phenomenon suggested the existence of an interaction between oxygen-containing groups in pomelo peel and iron species, which was well coincident with the analysis results from FTIR spectra in Figure S7. Beyond 700 °C, slight weight loss was observed, while an evident exothermal peak arose at 758 °C in the DSC curve, manifesting that it just involved the phase changes of iron species in the thermostable carbon matrix. Taking into consideration the above XRD and XPS results, the phase changes could be attributed to the transformation of θ-Fe_3C into α-Fe. On the whole, it was reasonable to choose 700 °C as the optimized carbonization temperature.

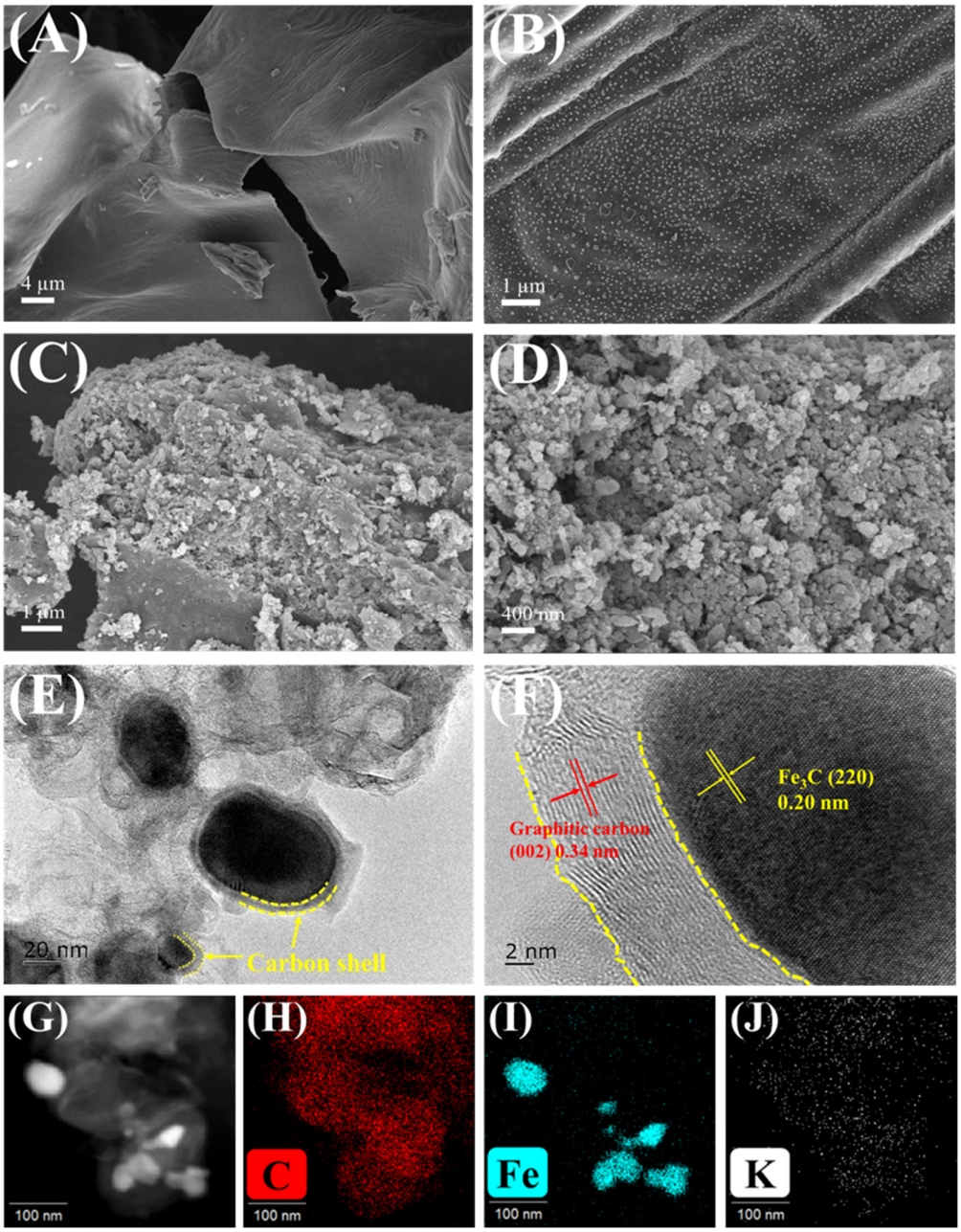

Figure 3. SEM images of (**A**) the dried pomelo peel, (**B**) the carbonized pomelo peel at 700 °C in N_2 flow and (**C**,**D**) the Fe@C-1.0 sample; (**E**,**F**) TEM and HRTEM images of the Fe@C-1.0 sample; (**G**–**J**) dark-field TEM image and corresponding elemental mapping of C, Fe, K on the Fe@C-1.0 sample.

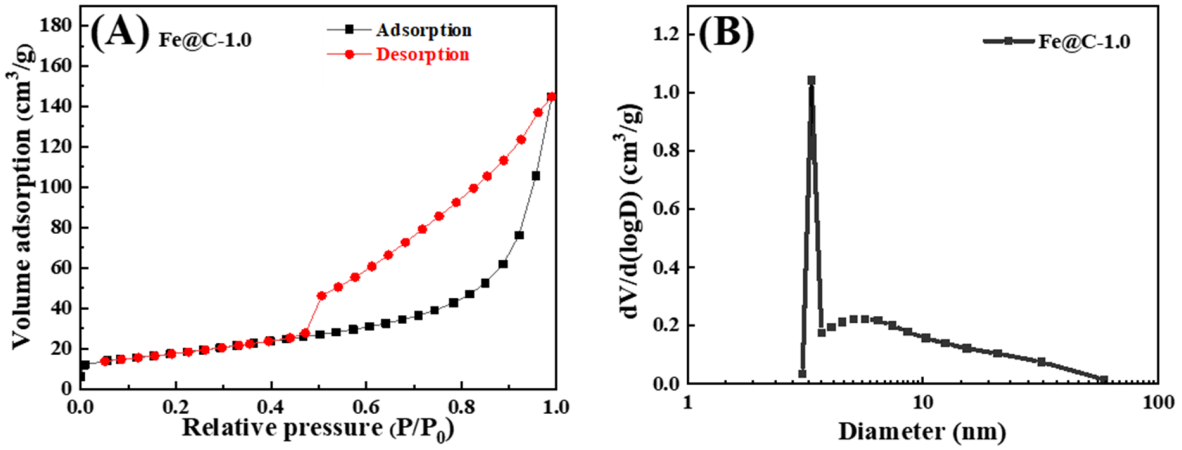

Figure 4. (**A**) N_2 adsorption/desorption isotherms and (**B**) pore size distributions of the Fe@C-1.0 sample.

Table 2. Typical textural properties of the as-prepared Fe@C-*x* samples.

Samples	Fe [a] (wt%)	K [a] (wt%)	Surface Area [b] ($m^2 \cdot g^{-1}$)	Pore Volume [b] ($cm^3 \cdot g^{-1}$)	Pore Diameter [b] (nm)	I_D/I_G [c]
Pomelo peel [e]	<0.1	1.1	0.6	<0.01	14.6	- [d]
Carbonized pomelo peel [f]	<0.1	3.9	1.5	<0.01	11.2	3.13
Fe@C-3.0	13.5	3.9	91.0	0.14	4.0	2.36
Fe@C-1.5	23.9	3.9	90.6	0.21	8.5	1.96
Fe@C-1.0	36.7	3.2	64.6	0.23	6.7	1.72
Fe@C-0.67	47.2	2.2	48.1	0.18	8.7	1.67

[a] Determined by ICP-OES. [b] Determined by the N_2 adsorption/desorption method. [c] Calculated from Raman spectra. [d] Not detected. [e] Pomelo peel dried at −50 °C for 24 h by freeze-drying method. [f] Prepared by carbonizing the dried pomelo peel at 700 °C in N_2 flow.

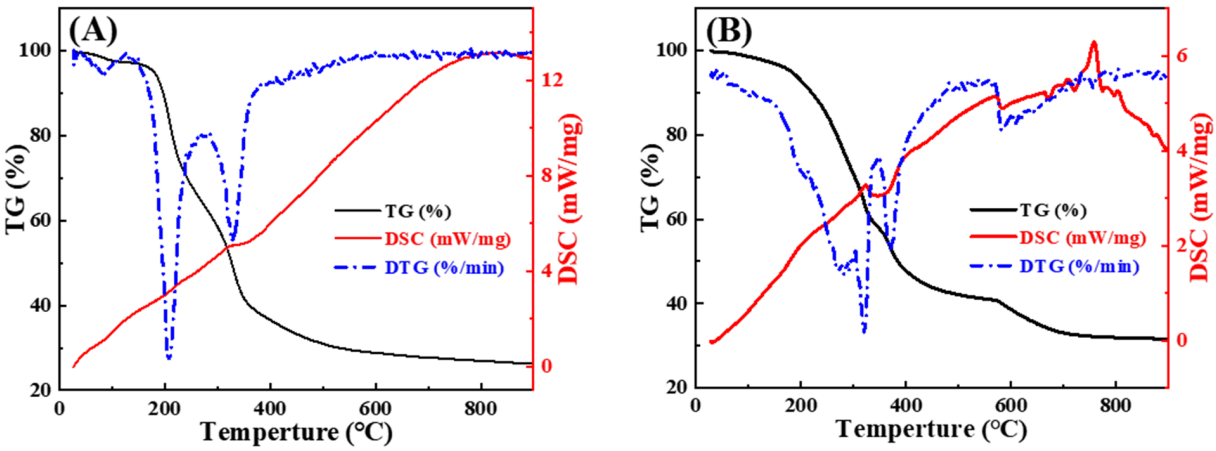

Figure 5. TG (black) and DSC (red) curves of (**A**) pomelo peel and (**B**) the precursor of Fe@C-1.0 after Fe impregnation.

2.2. Catalytic Performance of Fischer–Tropsch Synthesis

Initially, the FTS performance of the as-prepared Fe catalysts was screened for 24 h on stream over a fixed-bed reactor at 300 °C, 2.0 MPa, $H_2/CO = 1$ and GHSV = 3000 $mL \cdot g_{cat}^{-1} \cdot h^{-1}$. The FTS catalytic activities and product distributions of various Fe@C catalysts derived from pomelo peel are surveyed in Table 3 and Figure 6. To begin with, the comparative studies of catalytic activity were implemented on a series of K-Fe_3C@C nanohybrids with different Fe loadings. As a result, with ascending the Fe content from 8.0 wt% to 47.2 wt%,

the CO conversion firstly increased from 19.5% (8.0 wt%) to 92.6% (36.7 wt%), and then it progressively decreased to 79.2% (47.2 wt%). Meanwhile, the corresponding selectivity of methane (CH_4) and light paraffins (C_{2-4}) declined gradually, while the selectivity of C_{5+} hydrocarbons grew significantly, associated with the prominent O/P ratio of C_{2-4} in the range of 5.7–7.6. Interestingly, a volcano-like CO conversion profile was observed in Figure 6. After optimization, the Fe@C-1.0 catalyst achieved the maximum CO conversion of 92.6% and C_{5+} hydrocarbon selectivity of 61.3%, especially acquiring the satisfying light olefin ($C_{2-4}^{=}$) selectivity of 26.0% with the O/P ratio of 6.2. These phenomena suggested that the ascending Fe active sites could significantly facilitate the FTS activities, whereas beyond the optimum Fe loading of 36.7 wt%, the excessive Fe loading would generate immoderate aggregation of the Fe_3C nanoparticles, leading to the descending of CO conversion. Furthermore, the stability test of the Fe@C-1.0 catalyst on stream was evaluated for 100 h and is shown in Figure 7. The related testing results show that the pomelo-peel-derived Fe catalyst exhibited a satisfying long-term stability, as well as a sustained product selectivity to C_{5+} hydrocarbons and light olefins. The high performance for FTS was ascribed to the core-shell nanostructure composed of an Fe_3C active phase encapsulated by graphitized carbon shells [46,47]. Most importantly, the excellent olefin selectivity of the Fe@C-1.0 catalyst was explicitly relevant to the intrinsic organic and inorganic chemical compositions in pomelo peel, accumulating in the plant growth process [41,48]. After 24 h of the FTS reaction, the θ-Fe_3C active phase in the spent catalyst had no considerable transformation, characterized by XRD, FTIR, XPS and TEM in Figure S8 and Table S7.

Table 3. FTS catalytic activities of the Fe@C catalysts with different Fe loadings.

Catalysts	Fe [a] (wt%)	CO Conversion (%)	Selectivity of CO_2 (C%)	Hydrocarbon Selectivity (wt%, Free of CO_2)				C_{2-4} O/P [b]	α-Chain Growth Probability Factor [c]
				CH_4	C_{2-4}^{0}	$C_{2-4}^{=}$	C_{5+}		
Fe@C-6.0	8.0	19.5	63.3	22.5	8.0	45.7	23.8	5.7	- [d]
Fe@C-4.0	10.8	40.7	61.1	16.1	6.2	40.5	37.2	6.5	0.839
Fe@C-3.0	13.5	65.0	56.8	12.2	5.9	32.5	49.4	5.5	0.825
Fe@C-2.0	18.8	87.2	56.1	10.7	5.8	29.7	53.8	5.1	0.819
Fe@C-1.5	23.9	90.8	54.0	9.1	4.6	27.4	58.9	5.9	0.813
Fe@C-1.0	36.7	92.6	52.3	8.5	4.2	26.0	61.3	6.2	0.833
Fe@C-0.86	42.4	91.8	53.4	8.6	4.4	26.4	60.6	6.1	0.831
Fe@C-0.67	47.2	79.2	55.5	7.5	4.1	30.7	57.8	7.6	0.790

Reaction conditions: 300 °C, 2.0 Mpa, H_2/CO = 1 and GHSV = 3000 $mL \cdot g^{-1} \cdot h^{-1}$. Time on stream (TOS) = 24 h. [a] Determined by ICP-OES. [b] O/P means the mass ratio of olefin to paraffin. [c] According to the Anderson–Schulz–Flory distribution and Schulz formula $\ln(W_n/n) = n \ln\alpha + \ln((1-\alpha)^2/\alpha)$, the selectivity of heavy hydrocarbon increased with the increase in α. [d] The oil sample was too little to be detectable.

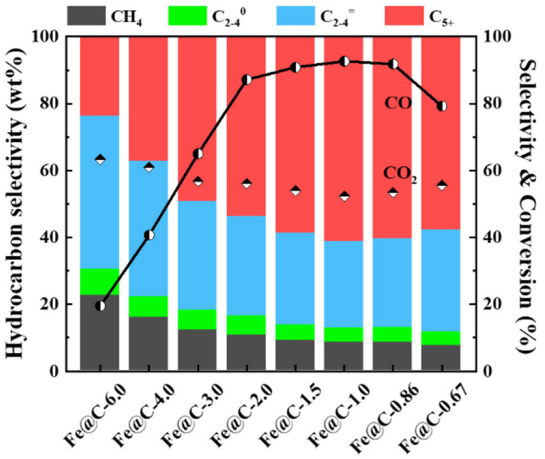

Figure 6. FTS catalytic activities of the Fe@C catalysts with different Fe loadings. Reaction conditions: 300 °C, 2.0 Mpa, H_2/CO = 1 and GHSV = 3000 $mL \cdot g^{-1} \cdot h^{-1}$. Time on stream (TOS) = 24 h.

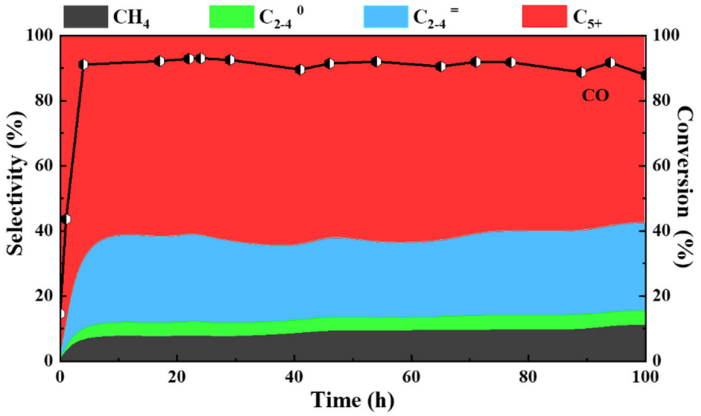

Figure 7. FTS stability test over the Fe@C-1.0 catalyst. Reaction conditions: 300 °C, 2.0 Mpa, H_2/CO = 1 and GHSV = 3000 $mL \cdot g^{-1} \cdot h^{-1}$.

To verify the effect of various biomass carbon sources on the FTS performance, a series of biomass-derived Fe@C nanohybrids were investigated in the FTS reaction. As shown in Figure 8 and Table S3, even consisting primarily of Fe_3C and α-Fe species, the variation in the type of biomass materials led to dramatic differences in the catalytic activity. Herein, the Fe@C catalysts made of rice straws and sugarcane bagasse exhibited an inferior performance with the higher C_{1-4} selectivity in hydrocarbon distribution up beyond 85% at a lower CO conversion of around 33%. Additionally, in the case of peanut shell, white gourd and watermelon peel, the corresponding catalysts possessed quite lower levels of CO conversion (0.5%–3.0%), in comparison to the pomelo-peel-derived catalyst (CO conversion of 65.0%). Considering three major constituents in lignocellulosic biomass, the natural carbon sources of xylose and filter paper contributed to the pronounced performance with the CO conversion above 80%, except for the negligible FTS activity corresponding to puffed rice and alkali lignin. In particular, in the series of biomass-based catalysts, the pomelo-peel-derived Fe catalyst accomplished a surprisingly high selectivity toward the higher formation of light olefins. As mentioned above, this favorable FTS performance was strongly associated with the occurrence of abundant inorganic metals such as potassium in biomass. In another aspect, the inherent sulfur could poison the iron-based catalysts availably, resulting in poor FTS performance, although sulfur generally exists only in small amounts in most terrestrial biomass [49]. As was evidenced in the previous literature and experimental results (Table S4), adding an extra sulfur source such as K_2S and protein powders could lead to the sharp decline or complete inactivation in the FTS activity in Table S5 [50].

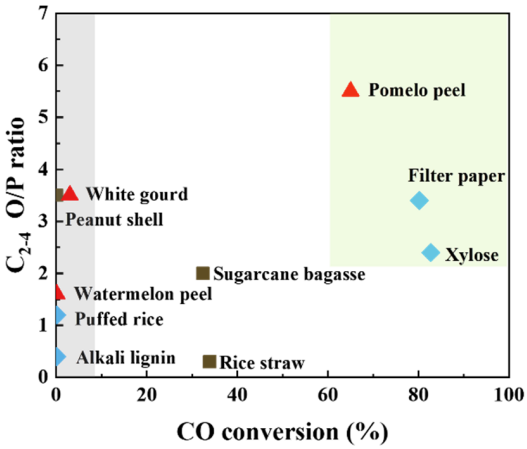

Figure 8. FTS catalytic activities of the Fe@C catalysts derived from different biomass materials. Reaction conditions: 300 °C, 2.0 MPa, H_2/CO = 1 and GHSV = 3000 $mL \cdot g^{-1} \cdot h^{-1}$.

More importantly, a range of designed experiments were carried out to verify the exact reason why the pomelo-peel-derived Fe catalysts exhibited an attractive FTS performance with a high selectivity toward C_{5+} hydrocarbons and light olefins. Out of all mineral elements existing in biomass waste, potassium is the second most absorbed nutrient in plant growth and metabolism. As expected in Table 2, the content of potassium in dried pomelo peel was 1.1 wt%, while that in the carbonized pomelo peel was significantly enhanced to 3.9 wt%. In particular, the Fe@C-1.0 catalyst comprised abundant potassium accounting for 3.2 wt%. As a well-known electronic donor, the potassium promoter could be conducive to suppressing the hydrogenation activity over iron active sites, resulting in a higher production of light olefins [51].

Thus, this synergetic effect between the inherent potassium and iron carbide species could be realized and certified repeatedly by the removal of potassium and follow-up incorporation of an extra potassium source, respectively. After the removal of potassium from the Fe@C-1.0 catalyst by washing in excess ultrapure water, the obtained sample was denoted as Fe@C-1.0-W, with a K residual of 0.1 wt% (Table 4). Subsequently, the so-called Fe@C-1.0-W-IM catalyst was achieved through impregnation of extra K_2CO_3 onto Fe@C-1.0-W in a mass ratio of 1:10. As described in Figure 9, it clearly proved that both of the as-prepared samples still maintained the same structural characteristics in the Fe@C-1.0 catalyst. More interestingly, the FTS performance on the Fe@C-1.0-W catalyst had substantially changed in the absence of K promoter, and the content of light paraffins (C_{1-4}) rose sharply while the O/P ratio value plummeted to a much lower level. After recovering the K enrichment on the catalyst surface, all of the characteristic values in the FTS performance were fully restored to normal. These variation trends exactly demonstrated that the K promoter was a key factor in influencing the trends of FTS product selectivity, which restricted the secondary hydrogenation of alkenes and led to more formation of light olefins and long-chain hydrocarbons [52,53].

Table 4. FTS catalytic activities of the K-doped catalysts with different preparation methods.

Catalysts	Fe [a] (wt%)	K [a] (wt%)	CO Conversion (%)	Selectivity of CO_2 (C%)	Hydrocarbon Selectivity (wt%, Free of CO_2)				C_{2-4} O/P	α-Chain Growth Probability Factor
					CH_4	$C_{2-4}{}^0$	$C_{2-4}{}^=$	C_{5+}		
Fe@C-1.0	36.7	3.2	92.6	52.3	8.5	4.2	26.0	61.3	6.2	0.833
Fe@C-1.0-W [b]	35.1	0.1	94.3	51.6	23.0	30.1	8.3	38.5	0.3	0.794
Fe@C-1.0-W-IM [c]	31.7	2.7	83.4	57.8	8.7	4.9	31.0	55.4	6.3	0.802

Reaction conditions: 300 °C, 2.0 MPa, H_2/CO = 1 and GHSV = 3000 $mL \cdot g^{-1} \cdot h^{-1}$. Time on stream (TOS) = 24 h. [a] Determined by ICP-OES. [b] Prepared by washing the Fe@C-1.0 catalyst with excess ultrapure water at least three times. [c] Prepared by impregnating Fe@C-1.0-W with K_2CO_3 solution in a mass ratio of 10:1 and then dried at 80 °C in an oven.

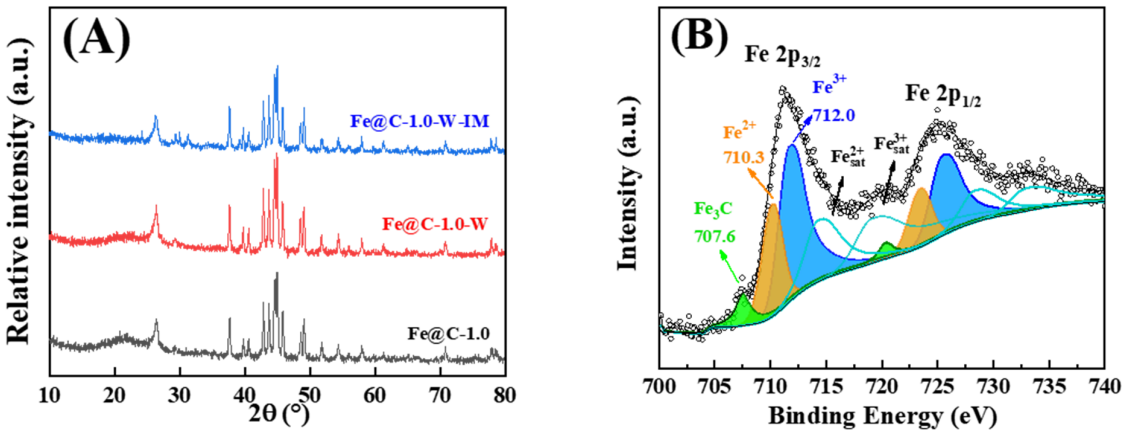

Figure 9. (**A**) XRD patterns of the K-doped catalysts with different preparation methods; (**B**) XPS survey spectra of Fe@C-1.0-W sample.

Overall, one extremely facile, green, low-cost synthetic strategy of high-performance FTS catalysts was successfully explored to in situ construct K-Fe_3C@C nanohybrids by using only ferric nitrate and pomelo peel without chemical pretreatment. In this strategy, pomelo peel, as a renewable carbon source and potassium source, provided abundant oxygen-containing functional organic components and inorganic minerals. Firstly, during the impregnation process, iron ions were coordinated with the oxygen-containing functional groups in pomelo peel, leading to the self-assembly into three-dimensional organic–inorganic hybrid precursors. Subsequently, during the carbonization process at 700 °C, the core-shell structural Fe_3C embedded in graphitic shells was in situ fabricated spontaneously, as a result of the decomposition and graphitization of the organic–inorganic hybrid precursors. Simultaneously, the potassium accumulated in pomelo peel also migrated and redistributed onto the surface of final nanohybrids. Hereinto, the effects of key factors including additive amounts of ferric nitrate, carbonization temperature, potassium doping and biomass types on the catalytic properties were systematically investigated. The corresponding physicochemical characteristics were carefully revealed by various analysis techniques, including XRD, BET, XPS, SEM/EDS, TEM, TG-DSC, ICP-OES, FTIR, Raman and Mössbauer measurements. Consequently, the calcination temperature of 700 °C was identified as the optimum carbonization condition for constructing a well-crystallized θ-Fe_3C phase. The biomass types chosen displayed a significant influence on the physicochemical properties and catalytic performance of the final products, originating from complex structural components and inorganic minerals. From FTS tests, a volcanic curve of CO conversion as a function of the iron loadings was observed, with the best FTS performance appearing at the iron loading of 47.2 wt%, which also corresponded to the mass ratio of 1.0 between dried pomelo peel and $Fe(NO_3)_3{\cdot}9H_2O$. Finally, the optimized K-Fe_3C@C catalysts revealed excellent FTS activity (92.6% CO conversion) with a highlighted C_{5+} hydrocarbon selectivity of 61.3% and light olefin ($C_{2\text{-}4}{}^{=}$) selectivity of 26.0% (olefin/paraffin (O/P) ratio of 6.2). A succession of experiments concerning potassium and corresponding analysis results of ICP-OES, XRD and XPS could verify that potassium promoter was the key reason why the pomelo-peel-derived Fe catalysts exhibited excellent FTS activity with high selectivity toward C_{5+} hydrocarbons and light olefins. The experimental results from the Fe@C catalysts doped with K_2S and protein powders clearly imply that the inherent rich sulfur element in biomass had a poisoning effect on the Fe active site, leading to low CO conversions.

To sum up, the Fe@C catalysts could be synthesized from natural biomass by this preparation method without chemical pretreatment or purification. However, as for the biomass-derived heterogeneous catalysts, it was necessary to consider the complex organic structural components and sulfur content accumulated in biomass and also pay attention to the roles of inherent inorganic elements performed in catalysts and the effects on catalytic performance.

3. Materials and Methods

3.1. Materials

Pomelo peel and other natural biomass materials were collected from local markets. All biomass was only cleaned with ultrapure water, freeze-dried and not chemically treated. Ferric nitrate ($Fe(NO_3)_3{\cdot}9H_2O$, 98.5%) and potassium bicarbonate (K_2CO_3, 99.5%) were purchased from Shanghai Macklin Biochemical Co., Ltd. (Shanghai, China). All the reagents were of analytical purity without any further purification.

3.2. Catalyst Preparation

The K-Fe_3C@C nanohybrids were directly fabricated through an extremely facile impregnation–carbonization process. In a typical preparation procedure (Figure S1), the obtained pomelo peel was firstly washed clean with ultrapure water and then processed with the vacuum freeze-drying stage (−50 °C) for 24 h. Prior to impregnation, the dried specimens were ground into powders (about 60–80 mesh) and stored in dry conditions to

avoid absorbing moisture. Next, appropriate amounts of $Fe(NO_3)_3 \cdot 9H_2O$ were dissolved in ultrapure water and impregnated into the dried powders (about 700 wt% of the water absorption rate). After standing for 12 h at room temperature, the impregnated samples were dried gradually at 80 °C for 72 h in an oven until the water was fully evaporated. Finally, the pretreated samples were directly carbonized at 700 °C for 2h with a heating rate of 10 °C/min under the protection of N_2. The as-prepared nanohybrids derived from pomelo peel were labeled as "Fe@C-*x*", where "*x*" indicated the mass ratio of dried pomelo peel to $Fe(NO_3)_3 \cdot 9H_2O$ during initial impregnation.

For comparison, other biomass materials were also selected as different natural carbon sources for fabricating Fe@C nanohybrids, such as crop straws (rice straw, rapeseed straw, corn stalk, peanut shell and sugarcane bagasse), fruit peels and pulps (orange peel, watermelon peel, white gourd and aloe pulp), hydrophyte (water moss and water hyacinth) and biomass-derived chemicals and materials (xylose, glucose, puffed rice, filter paper, microcrystalline cellulose and alkali lignin). The mass ratio of dried bio-materials to ferric nitrate equaled 3.0. The subsequent preparation process was performed in the same procedures described above. In the case of xylose and glucose, the precursors could be transformed into the fully dried gel before high-temperature pyrolysis.

3.3. Catalyst Characterization

The samples were characterized by X-ray diffraction (XRD), X-ray photoelectron spectra (XPS), scanning electron microscopy (SEM), transmission electron microscopy (TEM), N_2 adsorption and desorption isotherms and inductively coupled plasma–optical emission spectroscopy (ICP-OES) techniques. XRD patterns were recorded by Rigaku Smart Lab (3 kW, Tokyo, Japan) with Cu Kα radiation (λ = 0.154 nm) operated at 40 kV and 30 mA. SEM using MERLIN (Carl Zeiss, Oberkochen, Germany) and TEM using JEM-2100F (JEOL, Tokyo, Japan) were used to study the morphologies. Elemental analysis was carried out by ICP-OES (Agilent ICP-OES 720, Palo Alto, Santa Clara, CA, USA). The content of C, H, N and S elements was determined using elemental analyzer (Elementar Vario EL III, Hanau, Germany). XPS analysis was conducted with an ESCALAB 250Xi spectrometer (Thermo Electron Corp., Waltham, UK) with an Al Kα source (1486.6 eV), and all binding energies were corrected according to the C 1s peak at 284.8 eV. The specific surface area was calculated by the classical BET method at −196.15 °C using Micromeritics for ASAP 2460 (Norcross, GA, USA), and porosity properties were evaluated by BJH method. The ^{57}Fe Mössbauer spectra (MES) of the catalysts were carried out on a Topologic 500A spectrometer (Kanagawa, Japan) driving with a proportional counter at room temperature. The radioactive source was ^{57}Co (Rh) moving in a constant acceleration mode. Data analyses were performed assuming a Lorentzian line shape for computer folding and fitting. The components of iron phases were identified based on their Mössbauer parameters including isomer shift, quadruple splitting and magnetic hyperfine field. Thermogravimetric and differential scanning calorimetry (TG-DSC) was carried out on NETZSCH STA409PC instrument (Freistaat Bayern, Germany) with heating rate of 10 °C/min, temperature range from 26 °C to 900 °C in N_2 flow (40 mL/min).

3.4. Fischer–Tropsch Synthesis Reaction

The FTS reaction was performed in a fixed-bed tubular reactor (316L stainless steel, I.D. 10 mm). For each run, 1.0 g of catalyst diluted with 2.0 g of quartz sand (60–80 mesh) was loaded into the reactor, and in situ reduction was conducted under syngas flow ($H_2/CO/N_2$ = 47.5/47.5/5) at 300 °C, 0.1 MPa and GHSV = 3000 $mL \cdot g^{-1} \cdot h^{-1}$ (gas per hourly space velocity) for 12 h. Subsequently, the FTS performance of Fe@C catalysts was detected for a period of 24 h under operating conditions (300 °C, 2.0 MPa and 3000 $mL \cdot g^{-1} \cdot h^{-1}$). To estimate the stability of catalysts, the test of time on stream was performed for 100 h. In addition, the detailed analysis systems and chromatographic conditions were implemented consistently with the previous work (Figure S2) [12].

4. Conclusions

In summary, K-Fe_3C@C nanohybrids were effectively fabricated in situ by utilizing natural biomass waste of pomelo peel as a renewable carbon source and potassium source through an extremely facile route of high-temperature pyrolysis. During one-pot carbonization of the iron-impregnated pomelo peel, the decomposition and graphitization of its organic components not only contributed to the spontaneous formation of core-shell structural Fe_3C encapsulated in multilayer graphitic shells but also led to the migration and redistribution of potassium present in plant tissues onto the surface of as-synthesized nanohybrids. The key influencing parameters containing additive amounts of ferric nitrate, carbonization temperature and biomass types on the physicochemical characteristics of the pomelo-peel-derived Fe catalysts were primarily evaluated. Under the optimized condition, the self-assembled K-Fe_3C@C catalysts demonstrated high FTS activity (92.6% CO conversion) (Table S6), which selectively converted syngas to desired C_{2-4} olefin (26.0%) with a remarkable O/P ratio (6.2), as well as highlighted C_{5+} hydrocarbon (61.3%). The synergetic effect of core-shell structural Fe_3C and inherent potassium promoter was responsible for the high performance in controlling the transformation of syngas into desired light olefins and C_{5+} hydrocarbons. In particular, the surface enriched potassium, acting as an electronic donor to iron carbide, could contribute to restraining the hydrogenation activity of olefins and suppressing methane formation. As the renewable source of organic carbon and mineral potassium, pomelo peel was reported for the first time to be of great application potential in the fabrication of high-performance Fe-based FTS catalysts via the low-cost, green and scalable method. This construction strategy creates new opportunities for the design and utilization of natural biomass materials without any chemical treatment.

Supplementary Materials: The following supporting information can be downloaded at: https://www.mdpi.com/article/10.3390/catal12050542/s1, Figure S1: Schematic illustration of the preparation process for the typical Fe@C catalysts; Figure S2: The experimental setup of internally interconnected fixed-bed reactor system; Figure S3: XRD patterns of iron-impregnated different biomass materials carbonized at 700 °C; Figure S4: SEM-EDS images with of (A) carbonized pomelo peel and (B) Fe@C-1.0 sample; (C–E) TEM images and (F) HRTEM of Fe@C-1.0 sample; Figure S5: N_2 adsorption-desorption isotherms and pore size distributions of typical samples; Figure S6: Raman spectra of typical samples; Figure S7: FTIR spectra of (a) dried pomelo peel, (b) carbonized pomelo peel, (c) the precursor of Fe@C-1.0 after Fe-impregnation and (d) the Fe@C-1.0 sample; Figure S8: (A) XRD patterns and (B) FTIR spectra of Fe@C-1.0 sample and spent Fe@C-1.0 sample after 24 h on stream in FTS reaction test; (C) XPS survey spectra and (D–F) TEM images of spent Fe@C-1.0 sample after 24 h on stream in FTS reaction test; Table S1: Chemical compositions (percent of dry matter) of waste pomelo peel; Table S2: Detailed elemental contents of samples obtained by ICP-OES technique; Table S3: FTS catalytic activities of catalysts utilizing various biomass materials; Table S4: Typical elemental contents of the as-prepared Fe@C-1.0 and WP-1.0; Table S5: FTS catalytic activities of the Fe@C catalysts with different sulfur doping; Table S6: Comparison of FTS performance over various carbon-supported iron catalysts; Table. S7: Fe 2p orbital XPS data of Fe@C-1.0 and spent Fe@C-1.0. [11,26,50,54–69].

Author Contributions: S.Q.: writing—review and editing, funding acquisition. J.C.: conceptualization, methodology, resources, investigation, writing—original draft. Y.F.: methodology, resources. Z.H.: methodology, resources. Q.M.: investigation. L.M.: resources, investigation. Q.Z.: validation, formal analysis, supervision, funding acquisition. T.W.: supervision, funding acquisition. All authors have read and agreed to the published version of the manuscript.

Funding: This research was funded by the National Natural Science Foundation of China (51906048, 51876046), the Guangdong Basic and Applied Basic Research Foundation (2019A1515010416), the National Key Research and Development Program of China (2018YFE0125200) and the Guangdong Provincial Key Laboratory of Plant Resources Biorefinery (2021GDKLPRB05).

Conflicts of Interest: The authors declare no conflict of interest.

References

1. Davis, B.H. Fischer–Tropsch synthesis: Relationship between iron catalyst composition and process variables. *Catal. Today* **2003**, *84*, 83–98. [CrossRef]
2. Li, J.; He, Y.; Tan, L.; Zhang, P.; Peng, X.; Oruganti, A.; Yang, G.; Abe, H.; Wang, Y.; Tsubaki, N. Integrated tuneable synthesis of liquid fuels via Fischer–Tropsch technology. *Nat. Catal.* **2018**, *1*, 787–793. [CrossRef]
3. Teimouri, Z.; Abatzoglou, N.; Dalai, A.K. Kinetics and selectivity study of Fischer–Tropsch synthesis to C_{5+} hydrocarbons: A review. *Catalysts* **2021**, *11*, 330–361. [CrossRef]
4. Chang, Q.; Zhang, C.; Liu, C.; Wei, Y.; Cheruvathur, A.V.; Dugulan, A.I.; Niemantsverdriet, J.W.; Liu, X.; He, Y.; Qing, M.; et al. Relationship between iron carbide phases (ε-Fe_2C, Fe_7C_3, and χ-Fe_5C_2) and catalytic performances of Fe/SiO_2 Fischer–Tropsch catalysts. *ACS Catal.* **2018**, *8*, 3304–3316. [CrossRef]
5. Lin, Q.; Cheng, M.; Zhang, K.; Li, W.; Wu, P.; Chang, H.; Lv, Y.; Men, Z. Development of an iron-based Fischer–Tropsch catalyst with high attrition resistance and stability for industrial application. *Catalysts* **2021**, *11*, 908. [CrossRef]
6. Li, S.; Yang, J.; Song, C.; Zhu, Q.; Xiao, D.; Ma, D. Iron carbides: Control synthesis and catalytic applications in CO_x hydrogenation and electrochemical HER. *Adv. Mater.* **2019**, *31*, 176–188. [CrossRef]
7. Torres Galvis, H.M.; Bitter, J.H.; Khare, C.B.; Ruitenbeek, M.; Dugulan, A.I.; de Jong, K.P. Supported iron nanoparticles as catalysts for sustainable production of lower olefins. *Science* **2012**, *335*, 835–838. [CrossRef]
8. Zhao, S.; Liu, X.-W.; Huo, C.-F.; Li, Y.-W.; Wang, J.; Jiao, H. Determining surface structure and stability of ε-Fe_2C, χ-Fe_5C_2, θ-Fe_3C and Fe_4C phases under carburization environment from combined DFT and atomistic thermodynamic studies. *Catal. Struct. React.* **2014**, *1*, 44–60. [CrossRef]
9. Yang, X.; Zhang, H.; Liu, Y.; Ning, W.; Han, W.; Liu, H.; Huo, C. Preparation of iron carbides formed by iron oxalate carburization for Fischer–Tropsch synthesis. *Catalysts* **2019**, *9*, 347. [CrossRef]
10. Zhuo, O.; Yang, L.; Gao, F.; Xu, B.; Wu, Q.; Fan, Y.; Zhang, Y.; Jiang, Y.; Huang, R.; Wang, X.; et al. Stabilizing the active phase of iron-based Fischer–Tropsch catalysts for lower olefins: Mechanism and strategy. *Chem. Sci.* **2019**, *10*, 6083–6090. [CrossRef]
11. Ma, C.; Zhang, W.; Chang, Q.; Wang, X.; Wang, H.; Chen, H.; Wei, Y.; Zhang, C.; Xiang, H.; Yang, Y.; et al. θ-Fe_3C dominated Fe@C core–shell catalysts for Fischer–Tropsch synthesis: Roles of θ-Fe_3C and carbon shell. *J. Catal.* **2021**, *393*, 238–246. [CrossRef]
12. Zhang, Q.; Gu, J.; Chen, J.; Qiu, S.; Wang, T. Facile fabrication of porous Fe@C nanohybrids from natural magnetite as excellent Fischer–Tropsch catalysts. *Chem. Commun.* **2020**, *56*, 4523–4526. [CrossRef] [PubMed]
13. Tian, Y.; Xu, L.; Qian, J.; Bao, J.; Yan, C.; Li, H.; Li, H.; Zhang, S. Fe_3C/Fe_2O_3 heterostructure embedded in N-doped graphene as a bifunctional catalyst for quasi-solid-state zinc-air batteries. *Carbon* **2019**, *146*, 763–771. [CrossRef]
14. Xiong, H.; Moyo, M.; Motchelaho, M.A.; Tetana, Z.N.; Dube, S.M.A.; Jewell, L.L.; Coville, N.J. Fischer–Tropsch synthesis: Iron catalysts supported on N-doped carbon spheres prepared by chemical vapor deposition and hydrothermal approaches. *J. Catal.* **2014**, *311*, 80–87. [CrossRef]
15. Ye, Z.; Zhang, P.; Lei, X.; Wang, X.; Zhao, N.; Yang, H. Iron carbides and nitrides: Ancient materials with novel prospects. *Chem.-Eur. J.* **2018**, *24*, 8922–8940. [CrossRef]
16. Zhao, P.; Hua, X.; Xu, W.; Luo, W.; Chen, S.; Cheng, G. Metal–organic framework-derived hybrid of Fe_3C nanorod-encapsulated, N-doped CNTs on porous carbon sheets for highly efficient oxygen reduction and water oxidation. *Catal. Sci. Technol.* **2016**, *6*, 6365–6371. [CrossRef]
17. Arce-Saldaña, L.A.; Espinoza-Mosso, E.; Castro-Rodríguez, B.; Portillo-López, A.; Muñoz-Muñoz, F.; Dominguez, D.; Farías, M.H.; Soto, G. Plasma synthesis of carbon powder with embedded Fe_3C nanoparticles for magnetic separation of biomolecules. *Adv. Powder Technol.* **2018**, *29*, 1035–1041. [CrossRef]
18. Zhao, H.; Liu, J.; Yang, C.; Yao, S.; Su, H.; Gao, Z.; Dong, M.; Wang, J.; Hou, Y.; Li, W.; et al. Synthesis of iron-carbide nanoparticles: Identification of the active phase and mechanism of Fe-based Fischer–Tropsch synthesis. *CCS Chem.* **2021**, *3*, 2712–2724. [CrossRef]
19. Yao, S.; Yang, C.; Zhao, H.; Li, S.; Lin, L.; Wen, W.; Liu, J.; Hu, G.; Li, W.; Hou, Y.; et al. Reconstruction of the wet chemical synthesis process: The case of Fe_5C_2 nanoparticles. *J. Phys. Chem. C* **2017**, *121*, 5154–5160. [CrossRef]
20. De, S.; Balu, A.M.; van der Waal, J.C.; Luque, R. Biomass-derived porous carbon materials: Synthesis and catalytic applications. *ChemCatChem* **2015**, *7*, 1608–1629. [CrossRef]
21. Tang, Z.E.; Lim, S.; Pang, Y.L.; Ong, H.C.; Lee, K.T. Synthesis of biomass as heterogeneous catalyst for application in biodiesel production: State of the art and fundamental review. *Renew. Sustain. Energy Rev.* **2018**, *92*, 235–253. [CrossRef]
22. Wang, Z.; Shen, D.; Wu, C.; Gu, S. State-of-the-art on the production and application of carbon nanomaterials from biomass. *Green Chem.* **2018**, *20*, 5031–5057. [CrossRef]
23. Qin, H.; Zhou, Y.; Bai, J.; Zhu, B.; Ni, Z.; Wang, L.; Liu, W.; Zhou, Q.; Li, X. Lignin-derived thin-walled graphitic carbon-encapsulated iron nanoparticles: Growth, characterization, and applications. *ACS Sustain. Chem. Eng.* **2017**, *5*, 1917–1923. [CrossRef]
24. Schnepp, Z.; Wimbush, S.C.; Antonietti, M.; Giordano, C. Synthesis of highly magnetic iron carbide nanoparticles via a biopolymer route. *Chem. Mater.* **2010**, *22*, 5340–5344. [CrossRef]
25. Xiao, L.; Ye, F.; Zhou, Y.; Zhao, G. Utilization of pomelo peels to manufacture value-added products: A review. *Food Chem.* **2021**, *351*, 129247–129261. [CrossRef]

26. Oberoi, H.S.; Vadlani, P.V.; Nanjundaswamy, A.; Bansal, S.; Singh, S.; Kaur, S.; Babbar, N. Enhanced ethanol production from Kinnow mandarin (*Citrus reticulata*) waste via a statistically optimized simultaneous saccharification and fermentation process. *Bioresour. Technol.* **2011**, *102*, 1593–1601. [CrossRef]
27. Yongvanich, N. Isolation of nanocellulose from pomelo fruit fibers by chemical treatments. *J. Nat. Fibers* **2015**, *12*, 323–331. [CrossRef]
28. Zou, J.; Chai, W.; Liu, X.; Li, B.; Zhang, X.; Yin, T. Magnetic pomelo peel as a new absorption material for oil-polluted water. *Desalin. Water Treat.* **2015**, *57*, 12536–12545. [CrossRef]
29. Alva, A.K.; Mattos, D.; Paramasivam, S.; Patil, B.; Dou, H.; Sajwan, K.S. Potassium management for optimizing citrus production and quality. *Int. J. Fruit Sci.* **2006**, *6*, 3–43. [CrossRef]
30. Liang, Q.; Ye, L.; Huang, Z.H.; Xu, Q.; Bai, Y.; Kang, F.; Yang, Q.H. A honeycomb-like porous carbon derived from pomelo peel for use in high-performance supercapacitors. *Nanoscale* **2014**, *6*, 13831–13837. [CrossRef]
31. Peng, H.; Ma, G.; Sun, K.; Zhang, Z.; Yang, Q.; Lei, Z. Nitrogen-doped interconnected carbon nanosheets from pomelo mesocarps for high performance supercapacitors. *Electrochimica Acta* **2016**, *190*, 862–871. [CrossRef]
32. Peng, C.; Lang, J.; Xu, S.; Wang, X. Oxygen-enriched activated carbons from pomelo peel in high energy density supercapacitors. *RSC Adv.* **2014**, *4*, 54662–54667. [CrossRef]
33. Zhao, R.; Wang, Z.; Yang, Y.; Xing, X.; Zou, T.; Wang, Z.; Hong, P.; Peng, S.; Wang, Y. Pd-functionalized SnO_2 nanofibers prepared by shaddock peels as bio-templates for high gas sensing performance toward butane. *Nanomaterials* **2018**, *9*, 13–28. [CrossRef] [PubMed]
34. Ma, M.; You, S.; Wang, W.; Liu, G.; Qi, D.; Chen, X.; Qu, J.; Ren, N. Biomass-derived porous Fe_3C/tungsten carbide/graphitic carbon nanocomposite for efficient electrocatalysis of oxygen reduction. *ACS Appl. Mater. Interfaces* **2016**, *8*, 32307–32316. [CrossRef]
35. Wang, C.; Liu, Y.; Cui, Z.; Yu, X.; Zhang, X.; Li, Y.; Zhang, Q.; Chen, L.; Ma, L. In situ synthesis of Cu nanoparticles on carbon for highly selective hydrogenation of furfural to furfuryl alcohol by using pomelo peel as the carbon source. *ACS Sustain. Chem. Eng.* **2020**, *8*, 12944–12955. [CrossRef]
36. Zhao, S.; Wang, L.; Wang, Y.; Li, X. Hierarchically porous $LaFeO_3$ perovskite prepared from the pomelo peel bio-template for catalytic oxidation of NO. *J. Phys. Chem. Solids* **2018**, *116*, 43–49. [CrossRef]
37. Fan, G.; Jiang, Y.; Xin, J.; Zhang, Z.; Fu, X.; Xie, P.; Cheng, C.; Liu, Y.; Qu, Y.; Sun, K.; et al. Facile synthesis of Fe@Fe_3C/C nanocomposites derived from bulrush for excellent electromagnetic wave-absorbing properties. *ACS Sustain. Chem. Eng.* **2019**, *7*, 18765–18774. [CrossRef]
38. Cao, X.; Sun, S.; Sun, R. Application of biochar-based catalysts in biomass upgrading: A review. *RSC Adv.* **2017**, *7*, 48793–48805. [CrossRef]
39. Han, Y.; Fang, C.; Ji, X.; Wei, J.; Ge, Q.; Sun, J. Interfacing with carbonaceous potassium promoters boosts catalytic CO_2 hydrogenation of iron. *ACS Catal.* **2020**, *10*, 12098–12108. [CrossRef]
40. Lee, J.H.; Lee, H.K.; Kim, K.; Rhim, G.B.; Youn, M.H.; Jeong, H.; Park, J.H.; Chun, D.H.; Kim, B.-H.; Park, J.C. Unravelling the K-promotion effect in highly active and stable Fe_5C_2 nanoparticles for catalytic linear α-olefin production. *Mater. Adv.* **2021**, *2*, 1050–1058. [CrossRef]
41. Bai, J.; Qin, C.; Xu, Y.; Du, Y.; Ma, G.; Ding, M. Biosugarcane-based carbon support for high-performance iron-based Fischer–Tropsch synthesis. *iScience* **2021**, *24*, 102715–102721. [CrossRef] [PubMed]
42. van Lith, S.C.; Jensen, P.A.; Frandsen, F.J.; Glarborg, P. Release to the gas phase of inorganic elements during wood combustion. part 2: Influence of fuel composition. *Energy Fuel.* **2008**, *22*, 1598–1609. [CrossRef]
43. Dai, J.; Tian, S.; Jiang, Y.; Chang, Z.; Xie, A.; Zhang, R.; Li, C.; Yan, Y. Fe_3C/Fe/C magnetic hierarchical porous carbon with micromesopores for highly efficient chloramphenicol adsorption: Magnetization, graphitization, and adsorption properties investigation. *Ind. Eng. Chem. Res.* **2018**, *57*, 3510–3522. [CrossRef]
44. Zuo, P.; Duan, J.; Fan, H.; Qu, S.; Shen, W. Facile synthesis high nitrogen-doped porous carbon nanosheet from pomelo peel and as catalyst support for nitrobenzene hydrogenation. *Appl. Surf. Sci.* **2018**, *435*, 1020–1028. [CrossRef]
45. Li, Q.; Liu, F.; Zhang, L.; Nelson, B.J.; Zhang, S.; Ma, C.; Tao, X.; Cheng, J.; Zhang, X. In situ construction of potato starch based carbon nanofiber/activated carbon hybrid structure for high-performance electrical double layer capacitor. *J. Power Sources* **2012**, *207*, 199–204. [CrossRef]
46. Tu, J.L.; Ding, M.Y.; Zhang, Q.; Zhang, Y.L.; Wang, C.G.; Wang, T.J.; Ma, L.L.; Li, X.J. Design of carbon-encapsulated Fe_3O_4 nanocatalyst with enhanced performance for Fischer–Tropsch synthesis. *ChemCatChem* **2015**, *7*, 2323–2327. [CrossRef]
47. Song, F.; Yong, X.; Wu, X.; Zhang, W.; Ma, Q.; Zhao, T.; Tan, M.; Guo, Z.; Zhao, H.; Yang, G.; et al. FeMn@HZSM-5 capsule catalyst for light olefins direct synthesis via Fischer–Tropsch synthesis: Studies on depressing the CO_2 formation. *Appl. Catal. B Environ.* **2022**, *300*, 120713–120722. [CrossRef]
48. Guo, L.; Sun, J.; Ji, X.; Wei, J.; Wen, Z.; Yao, R.; Xu, H.; Ge, Q. Directly converting carbon dioxide to linear α-olefins on bio-promoted catalysts. *Commun. Chem.* **2018**, *1*, 51–59. [CrossRef]
49. de Smit, E.; Weckhuysen, B.M. The renaissance of iron-based Fischer–Tropsch synthesis: On the multifaceted catalyst deactivation behaviour. *Chem. Soc. Rev.* **2008**, *37*, 2758–2781. [CrossRef]
50. Xu, J.D.; Chang, Z.Y.; Zhu, K.T.; Weng, X.F.; Weng, W.Z.; Zheng, Y.P.; Huang, C.J.; Wan, H.L. Effect of sulfur on α-Al_2O_3-supported iron catalyst for Fischer–Tropsch synthesis. *Appl. Catal. A Gen.* **2016**, *514*, 103–113. [CrossRef]

51. Amoyal, M.; Vidruk-Nehemya, R.; Landau, M.V.; Herskowitz, M. Effect of potassium on the active phases of Fe catalysts for carbon dioxide conversion to liquid fuels through hydrogenation. *J. Catal.* **2017**, *348*, 29–39. [CrossRef]
52. Gong, J.; Cao, C.; Sun, R.; Cui, L.; Gao, R.; Hao, H. A DFT insight into the tuning effect of potassium promoter on the formation of carbon atoms via carburization gases dissociation on iron-based catalysts. *Catalysts* **2020**, *10*, 527. [CrossRef]
53. Tian, Z.; Wang, C.; Yue, J.; Zhang, X.; Ma, L. Effect of a potassium promoter on the Fischer–Tropsch synthesis of light olefins over iron carbide catalysts encapsulated in graphene-like carbon. *Catal. Sci. Technol.* **2019**, *9*, 2728–2741. [CrossRef]
54. Qiu, T.; Wang, L.; Lv, S.; Sun, B.; Zhang, Y.; Liu, Z.; Yang, W.; Li, J. SAPO-34 zeolite encapsulated Fe_3C nanoparticles as highly selective Fischer–Tropsch catalysts for the production of light olefins. *Fuel* **2017**, *203*, 811–816. [CrossRef]
55. Li, J.; Yu, F.; Wang, M.; Lai, Y.; Wang, H.; Lei, X.; Fang, J. Highly dispersed iron nitride nanoparticles embedded in N doped carbon as a high performance electrocatalyst for oxygen reduction reaction. *Int. J. Hydrogen Energy* **2017**, *42*, 2996–3005. [CrossRef]
56. Huang, R.; Cao, M.; Guo, H.; Qi, W.; Su, R.; He, Z. Enhanced ethanol production from pomelo peel waste by integrated hydrothermal treatment, multienzyme formulation, and fed-batch operation. *J. Agric. Food Chem.* **2014**, *62*, 4643–4651. [CrossRef]
57. Rivas, B.; Torrado, A.; Torre, P.; Converti, A.; Domínguez, J.M. Submerged citric acid fermentation on orange peel autohydrolysate. *J. Agric. Food Chem.* **2008**, *56*, 2380–2387. [CrossRef]
58. Patsalou, M.; Samanides, C.G.; Protopapa, E.; Stavrinou, S.; Vyrides, I.; Koutinas, M. A Citrus peel waste biorefinery for ethanol and methane production. *Molecules* **2019**, *24*, 2451–2466. [CrossRef]
59. Chai, W.; Liu, X.; Zou, J.; Zhang, X.; Li, B.; Yin, T. Pomelo peel modified with acetic anhydride and styrene as new sorbents for removal of oil pollution. *Carbohydr. Polym.* **2015**, *132*, 245–251. [CrossRef]
60. Park, H.; Youn, D.H.; Kim, J.Y.; Kim, W.Y.; Choi, Y.H.; Lee, Y.H.; Choi, S.H.; Lee, J.S. Selective formation of Hägg iron carbide with g-C_3N_4 as a sacrificial support for highly active Fischer–Tropsch synthesis. *ChemCatChem* **2015**, *7*, 3488–3494. [CrossRef]
61. Schulte, H.J.; Graf, B.; Xia, W.; Muhler, M. Nitrogen- and oxygen-functionalized multiwalled carbon nanotubes used as support in iron-catalyzed, high-temperature Fischer–Tropsch synthesis. *ChemCatChem* **2012**, *4*, 350–355. [CrossRef]
62. Wu, J.; Wang, L.; Lv, B.; Chen, J. Facile fabrication of BCN nanosheet-encapsulated nano-iron as highly stable Fischer–Tropsch synthesis catalyst. ACS Appl. Mater. *Interfaces* **2017**, *9*, 14319–14327.
63. Yan, Q.; Wan, C.; Liu, J.; Gao, J.; Yu, F.; Zhang, J.; Cai, Z. Iron nanoparticles in situ encapsulated in biochar-based carbon as an effective catalyst for the conversion of biomass-derived syngas to liquid hydrocarbons. *Green Chem.* **2013**, *15*, 1631–1641. [CrossRef]
64. Jiang, F.; Liu, B.; Li, W.; Zhang, M.; Li, Z.; Liu, X. Two-dimensional graphene-directed formation of cylindrical iron carbide nanocapsules for Fischer–Tropsch synthesis. *Catal. Sci. Technol.* **2017**, *7*, 4609–4621. [CrossRef]
65. Gu, B.; He, S.; Zhou, W.; Kang, J.; Cheng, K.; Zhang, Q.; Wang, Y. Polyaniline-supported iron catalyst for selective synthesis of lower olefins from syngas. *J. Energy Chem.* **2017**, *26*, 608–615. [CrossRef]
66. Xie, J.; Galvis, H.M.T.; Koeken, A.C.J.; Kirilin, A.; Dugulan, A.I.; Ruitenbeek, M.; de Jong, K.P. Size and promoter effects on stability of carbon-nanofiber-supported iron-based Fischer–Tropsch catalysts. *ACS Catal.* **2016**, *6*, 4017–4024. [CrossRef]
67. Bahome, M.C.; Jewell, L.L.; Padayachy, K.; Hildebrandt, D.; Glasser, D.; Datye, A.K.; Coville, N.J. Fe-Ru small particle bimetallic catalysts supported on carbon nanotubes for use in Fischer–Tropsch synthesis. *Appl. Catal. A-Gen.* **2007**, *328*, 243–251. [CrossRef]
68. Tian, Z.; Wang, C.; Si, Z.; Ma, L.; Chen, L.; Liu, Q.; Zhang, Q.; Huang, H. Fischer–Tropsch synthesis to light olefins over iron-based catalysts supported on $KMnO_4$ modified activated carbon by a facile method. *Appl. Catal. A-Gen.* **2017**, *541*, 50–59. [CrossRef]
69. Zhao, X.; Lv, S.; Wang, L.; Li, L.; Wang, G.; Zhang, Y.; Li, J. Comparison of preparation methods of iron-based catalysts for enhancing Fischer–Tropsch synthesis performance. *Mol. Catal.* **2018**, *449*, 99–105. [CrossRef]